Physics of eccentric binary black hole mergers: A numerical relativity perspective

E. A. Huerta,[1,2] Roland Haas,[1] Sarah Habib,[1,3] Anushri Gupta,[1,2] Adam Rebei,[1,4] Vishnu Chavva,[1,3] Daniel Johnson,[1,5] Shawn Rosofsky,[1,3] Erik Wessel,[1,6] Bhanu Agarwal,[1,7] Diyu Luo,[1,8] and Wei Ren[1,9]

[1]*NCSA, University of Illinois at Urbana-Champaign, Urbana, Illinois 61801, USA*
[2]*Department of Astronomy, University of Illinois at Urbana-Champaign, Urbana, Illinois 61801, USA*
[3]*Department of Physics, University of Illinois at Urbana-Champaign, Urbana, Illinois 61801, USA*
[4]*The University of Illinois Laboratory High School, University of Illinois at Urbana-Champaign, Urbana, Illinois 61801, USA*
[5]*Institute for Computational and Mathematical Engineering, Stanford University, Stanford, California 94305, USA*
[6]*Department of Physics, University of Arizona, Tucson, Arizona 85721, USA*
[7]*Microsoft, One Microsoft Way, Redmond, Washington 98052, USA*
[8]*Oracle Corporation, Seattle, Washington 98101, USA*
[9]*Department of Electrical and Computer Engineering, University of Illinois at Urbana-Champaign, Urbana, Illinois 61801, USA*

(Received 23 January 2019; published 4 September 2019)

Gravitational wave observations of eccentric binary black hole mergers will provide unequivocal evidence for the formation of these systems through dynamical assembly in dense stellar environments. The study of these astrophysically motivated sources is timely in view of electromagnetic observations, consistent with the existence of stellar mass black holes in the globular cluster M22 and in the galactic center, and the proven detection capabilities of ground-based gravitational wave detectors. In order to get insights into the physics of these objects in the dynamical, strong-field gravity regime, we present a catalog of 89 numerical relativity waveforms that describe binary systems of nonspinning black holes with mass ratios $1 \leq q \leq 10$, and initial eccentricities as high as $e_0 = 0.18$ fifteen cycles before merger. We use this catalog to quantify the loss of energy and angular momentum through gravitational radiation, and the astrophysical properties of the black hole remnant, including its final mass and spin, and recoil velocity. We discuss the implications of these results for gravitational wave source modeling, and the design of algorithms to search for and identify eccentric binary black hole mergers in realistic detection scenarios.

DOI: 10.1103/PhysRevD.100.064003

I. INTRODUCTION

The gravitational wave (GW) detection of several binary black hole (BBH) mergers [1–6] and the first multimessenger observation of two colliding neutron stars (NSs) in gravitational and electromagnetic waves [7] have shed light into the nature of gravity in the most extreme astrophysical settings, and have unveiled the identity of the central engines that power the most energetic electromagnetic explosions in the Universe [8–11], while also providing the means to put at work visionary methods to use GWs to quantify the rate of expansion of the Universe [12–15].

Along this trail of discovery, it has also become evident that numerical relativity (NR) plays a central role to understand the physics of GW sources, and to inform the development of signal-processing algorithms to detect and characterize these astrophysical events [16–21], and astrophysical sources that still await discovery [22–36].

In preparation for the characterization of BBH mergers whose astrophysical properties span a parameter space that has not yet been probed by existing GW detections, several NR groups are working in earnest to construct large-scale NR waveform catalogs [17,37,38]. Since these activities have thus far focused on the study of quasicircular BBH mergers, in this article we fill in a critical void in the literature by presenting a comprehensive study of the physics of moderately eccentric BBH mergers.

The rationale for this study is multifold. From the perspective of electromagnetic observations, recent findings are consistent with the existence of stellar-mass BHs in the vicinity of the galactic center, and in the galactic cluster M22 [39–42]. These observations have triggered the development of numerical models that provide a realistic description of the formation and retention of BBHs in dense stellar environments, correcting previous calculations based on N-body simulations that did not include post-Newtonian corrections [43] to model the orbital dynamics

of these systems, thereby underestimating the merger rates of these systems by orders of magnitude [42,44–79]. In summary, we have evidence for the existence of stellar-mass BHs that may form eccentric compact binary systems in dense stellar environments, and consequently be detected through GW emission. Through this study, we provide new insights into the physics of these astrophysically motivated sources.

Furthermore, as discussed in [80], no matched-filtering algorithm has been presented in the literature that is tailored for the detection of $\ell = |m| = 2$ eccentric waveforms [80]. However, signal processing algorithms based on deep neural networks have been used to demonstrate that moderately eccentric BBH mergers can be detected and characterized from real LIGO noise, considering both NR waveforms that only include the leading order quadrupole mode $\ell = |m| = 2$ [22–25], and higher-order waveform multipoles [27]. We expect that this NR waveform catalog may be used to quantify the sensitivity of burst searches and of next-generation neural network models that are tailored to detect and characterize eccentric BBH mergers. In summary, activities around modeling, detection, and characterization of eccentric BBHs are reaching the required level of maturity to establish or rule out the existence of compact binary populations in dense stellar environments.

To advance our understanding of the physics of compact binary populations in dense stellar environments, in this article we introduce a NR waveform catalog that describes eccentric BBH mergers, and we utilize it to get insights into the dynamics of these GW sources, e.g., the energy and angular momentum loss through GW emission, and the astrophysical properties of the BH remnant, i.e., its final mass and spin as a function of initial eccentricity and mass ratio, as well as the recoil velocity of the BH remnant. These studies will inform ongoing GW modeling efforts and the development of signal-processing algorithms to search for and identify these sources. This article is organized as follows. Section II describes the properties of our NR catalog. In Sec. III we compute the energy and angular momentum radiated away through GW emission, making pairwise comparisons between NR waveforms that include the $\ell = |m| = 2$ mode or higher-order waveform multipoles. In Sec. IV we compute the astrophysical properties of the BH remnants and compare these results with those obtained for quasicircular BBH mergers. We describe the relevance of these analyses in terms of GW modeling efforts for eccentric BBH mergers in Sec. V. We summarize our findings and outline future directions of work in Sec. VI.

II. NUMERICAL RELATIVITY CATALOG

We have produced a catalog of 89 simulations with the open source, NR software, the EINSTEIN TOOLKIT [81–100]. This catalog describes nonspinning BBHs with mass ratios $1 \leq q \leq 10$ and eccentricities as high as $e_0 = 0.18$ fifteen cycles before merger. A visualization of this catalog may be found at [101,102]. We have postprocessed the data products of these simulations using the open source software stack POWER [103] and extracted the modes $(\ell, |m|) = \{(2,2), (2,1), (3,3), (3,2), (3,1), (4,4), (4,3), (4,2), (4,1)\}$. As described in Appendix B, each of these simulations was produced with several levels of resolution to quantify convergence. The real part of the $\ell = |m| = 2$ mode, extracted at future null infinity, for each NR waveform is presented in Fig. 1. The properties of these NR waveforms are listed in Table II.

Characterizing the properties of the NR waveforms presented in Table II requires the construction of a method to quantify the orbital eccentricity of these simulations. Using the orbital evolution of these simulations to obtain an estimate of the orbital eccentricity is inadequate due to the gauge-dependent nature of the binary's orbit. On the other hand, methods to construct initial data for spinning BHs on quasicircular orbits have also introduced definitions of orbital eccentricity, based on orbital separations and waveform phase and amplitude of the Weyl scalar ψ_4 [104]. However, while the scope of the method introduced in [104] is to construct high-quality initial data for quasicircular mergers, and therefore, using $\mathcal{O}(e)$ approximations to model the effect of eccentricity may suffice, we aim to measure larger values of orbital eccentricity.

To address this matter, we have used the inspiral-merger-ringdown ENIGMA waveform model introduced in [26] to determine the eccentricity, mean anomaly, and gauge-invariant frequency parameters, (e_0, ℓ_0, x_0), that optimally describe each NR waveform in our catalog. We do this by finding the (e_0, ℓ_0, x_0) triplet that maximizes the overlap between each NR waveform and its ENIGMA counterpart. In [105] we quantified the optimal time window to remove junk radiation while keeping intact the signatures of eccentricity at early times in the NR waveforms. Such time range is given by $t \leq 60M$. A detailed description of this method, including the corresponding open source software stack for its use to characterize NR waveforms catalogs at scale, is presented in an accompanying article [105].

In brief, we construct our method using the inspiral evolution of the ENIGMA waveform model, which contains state-of-the-art post-Newtonian corrections for eccentric binaries, which include eccentricity corrections in the conservative and radiative pieces up $\mathcal{O}(e^{12})$, including instantaneous, tails, and tails-of-tails contributions, and a contribution due to nonlinear memory; and quasicircular corrections both from post-Newtonian, self-force, and perturbative calculations up to $\mathcal{O}(x^6)$ [26,29]. Furthermore, in [26], we have demonstrated that $e_0 = 0$ ENIGMA waveforms capture the dynamics of quasicircular BBH mergers with excellent accuracy. We showed this by computing overlaps between quasicircular ENIGMA waveforms and their quasicircular effective one body (EOB)

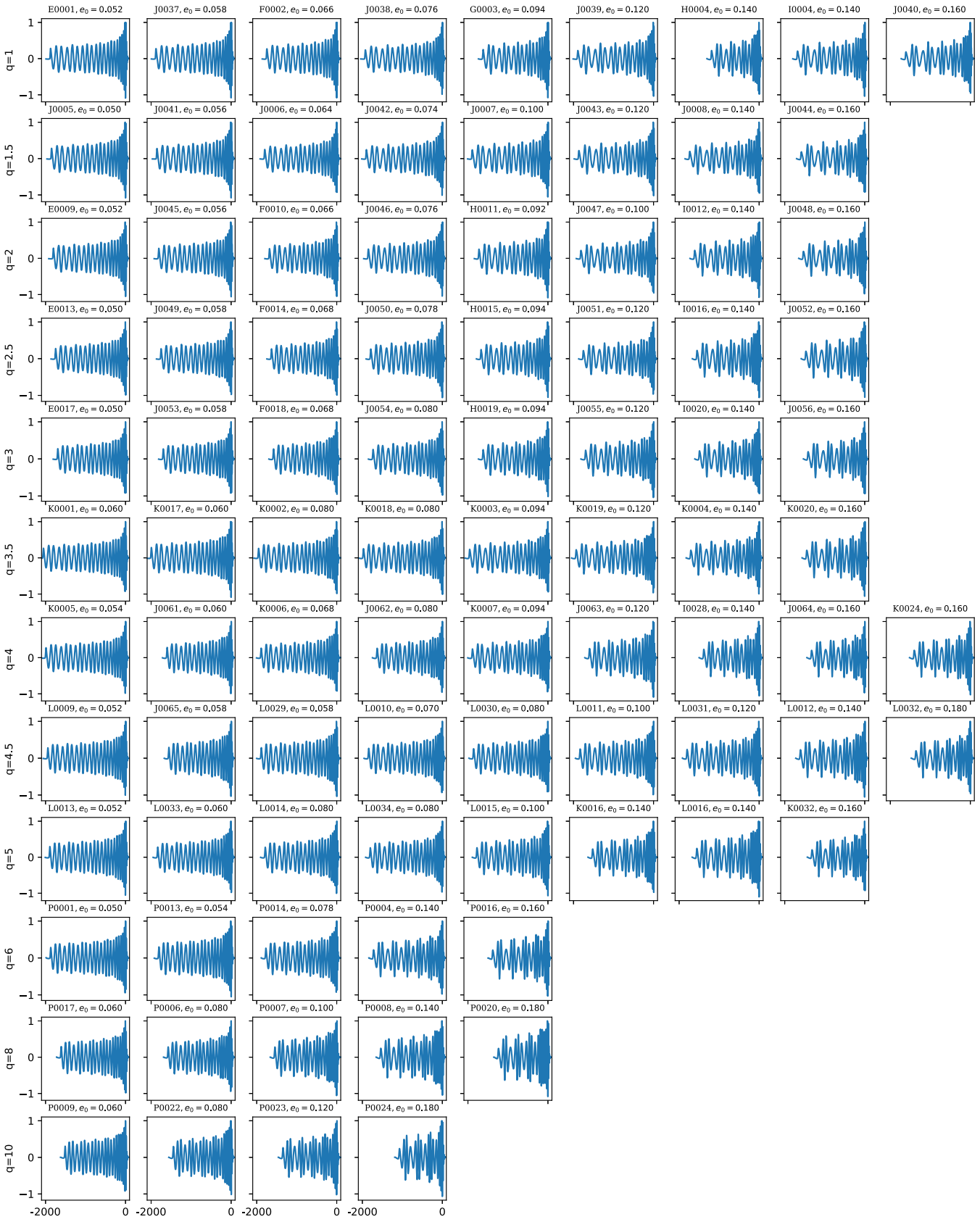

FIG. 1. For a given mass ratio q, each row presents the real part of the $\ell = |m| = 2$ mode of each waveform in our catalog, extracted at future null infinity. The initial eccentricity, e_0, increases from left to right. All these waveforms have unit amplitude at $t = 0$. Table II lists the properties of this waveform catalog.

counterparts [106]. Assuming advanced LIGO's zero detuned high power sensitivity [107], and using an initial GW frequency of 15 Hz to compute the overlaps, Fig. 2 in [26] shows that the overlap between quasicircular ENIGMA and EOB waveforms is $\mathcal{O} \geq 0.99$. Since the waveforms we are characterizing in this study are much shorter than those used to assess the accuracy of the ENIGMA model in the quasicircular limit, it follows that ENIGMA will capture the dynamics of moderately eccentric systems with excellent accuracy.

It is worth highlighting that while the ENIGMA waveform model was originally *validated* with eccentric NR waveforms that describe BBH mergers with mass ratios $q \leq 5.5$ and eccentricities $e_0 \leq 0.18$ twenty cycles before merger [26], it is through this analysis, and with the availability of new NR waveforms, that we can now report that the ENIGMA model can accurately describe BBH mergers with mass ratios up to $q = 10$ with $e_0 \leq 0.18$ fifteen cycles before merger.

III. ENERGY AND ANGULAR MOMENTUM EMISSION OF ECCENTRIC BLACK HOLE MERGERS

For each NR waveform in our catalog, we have quantified the energy, E, and angular momentum, J, radiated away through GW emission using the relations [108]

$$\Delta E = \frac{1}{16\pi} \int_{t_0}^{t} \sum_{m=-\ell}^{\ell} \sum_{\ell=2}^{\ell_{\rm max}} \mathrm{d}t' |N_{\ell m}(t')|^2, \tag{1}$$

$$\Delta J = \frac{1}{16\pi} \int_{t_0}^{t} \sum_{m=-\ell}^{\ell} \sum_{\ell=2}^{\ell_{\rm max}} \mathrm{d}t' m \Im[h_{\ell m}(t') N^*_{\ell m}(t')], \tag{2}$$

$$N_{\ell m}(t) = \frac{\mathrm{d}h_{\ell m}(t)}{\mathrm{d}t}, \tag{3}$$

where $N^{\ell m}(t)$ represents the complex *news function* at infinity. The integration is done from the time the NR waveform is free from junk radiation, $t_0 = 60M$, to the final sample time of the NR waveform, t. For these calculations we have considered the $(\ell, |m|) = \{(2,2), (2,1), (3,3), (3,2), (3,1), (4,4), (4,3), (4,2), (4,1)\}$ modes. It is worth pointing out that the choice $t_0 \to 60M$ is informed by the study presented in [105], which demonstrated that this choice removes high-frequency noise while keeping intact the imprints of eccentricity in the NR waveforms once they are free from junk radiation. Using Eqs. (1)–(3), in Fig. 2 we quantify the importance of including higher-order waveform modes to compute the energy and angular momentum carried away by GWs. We do this through pairwise comparisons between NR waveforms that include either all the modes listed above, or just the $\ell = |m| = 2$ mode, using the relations

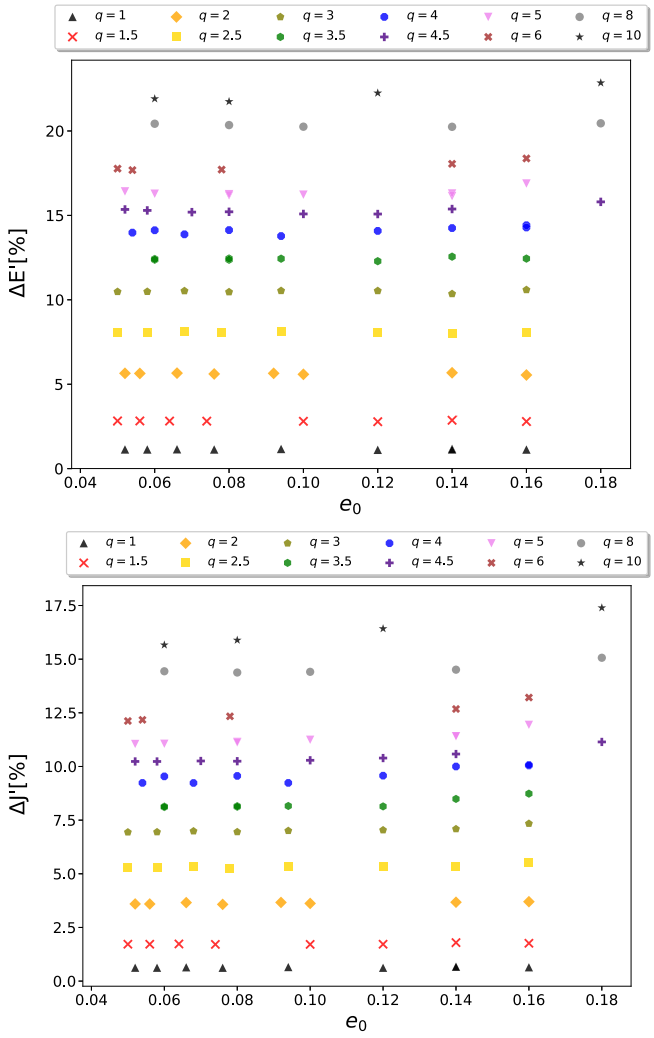

FIG. 2. Top panel: pairwise comparison in radiated energy between NR waveforms that include either all $(\ell, |m|)$ modes or just the $\ell = |m| = 2$ mode, as described by $\Delta E'$ in Eq. (4). Bottom panel: similar to the top panel, but now for radiated angular momentum, given by $\Delta J'$ in Eq. (5).

$$\Delta E' = \frac{\Delta E(\ell, |m|) - \Delta E(\ell = |m| = 2)}{\Delta E(\ell, |m|)}, \tag{4}$$

$$\Delta J' = \frac{\Delta J(\ell, |m|) - \Delta J(\ell = |m| = 2)}{\Delta J(\ell, |m|)}. \tag{5}$$

Using the two highest resolution runs for each simulation in our catalog, we computed $(\Delta E', \Delta J')$ and found that the largest difference between these two independent measurements is $\lesssim 5\%$. The values we present in Fig. 2 were extracted from the highest resolution runs. We notice that for each mass-ratio BBH population, i.e., if we consider a given set of markers in the panels of Fig. 2, $(\Delta E', \Delta J')$ are nearly constant across the eccentricity range that we have explored in this study. In different words, $(\Delta E', \Delta J')$ are constant polynomials

in eccentricity for $e_0 \leq 0.2$. We observe a minor deviation from this pattern at the high end of the eccentricity range for the most asymmetric mass-ratio BBH systems. To be precise, if we fit a constant polynomial using the two lowest eccentricity samples for each mass-ratio population, we find that the largest deviation occurs for the most eccentric sample of the $q = 10$ BBHs, with a fractional error $\lesssim 8\%$ for the measurement of $\Delta J'$.

These results also show that for systems with $q \geq 5$ it is essential to include higher-order waveform modes to accurately describe the dynamics of eccentric BBH mergers. This result is consistent with recent studies [27], which indicate that the inclusion of higher-order modes for nonspinning, eccentric BBH mergers has a more significant impact for GW detection, in the context of signal-to-noise ratio calculations, than for their nonspinning, quasicircular BBH counterparts. It is worth highlighting that the eccentric NR waveforms we have produced for this analysis for $q \geq 5$ are the first of their kind in the literature, so these results shed new light on the importance of including higher-order waveform modes for the modeling of radiated energy and angular momentum of eccentric BBH mergers.

IV. FINAL MASS, SPIN, AND RECOIL VELOCITY OF POSTMERGER BLACK HOLES

We have computed the final mass, M_f, and final spin, q_f, of the BH remnant using the QuasiLocalMeasures thorn of the Einstein Toolkit. The final mass is given by

$$M_f = \sqrt{M_{\rm irr}^2 + \frac{q_f^2}{4M_{\rm irr}}}, \quad \text{where} \tag{6}$$

$$M_{\rm irr} = \sqrt{\frac{A}{16\pi}}, \tag{7}$$

$M_{\rm irr}$ is the irreducible mass, given in terms of the BHs' event horizon area, A. q_f is computed as the Komar angular momentum [109–112]

$$q_f = \frac{1}{8\pi} \oint_S K_{ij} s^i \phi^j dA, \tag{8}$$

where the integral is over the surface, S, of the apparent horizon, K_{ij} is the extrinsic curvature, s^i is a spacelike, outward normal to the horizon, and ϕ^i is a Killing vector associated with the rotational symmetry around the spin axis.

In Fig. 3 we present results for (M_f, q_f). As before, we used our two highest resolution runs for each NR simulation to compute these observables and found that these two independent measurements differ by $\lesssim 3\%$. The results presented for (M_f, q_f) in Fig. 3 were extracted from the highest resolution runs in our catalog. We notice that for each mass-ratio population, i.e., for a given set of markers,

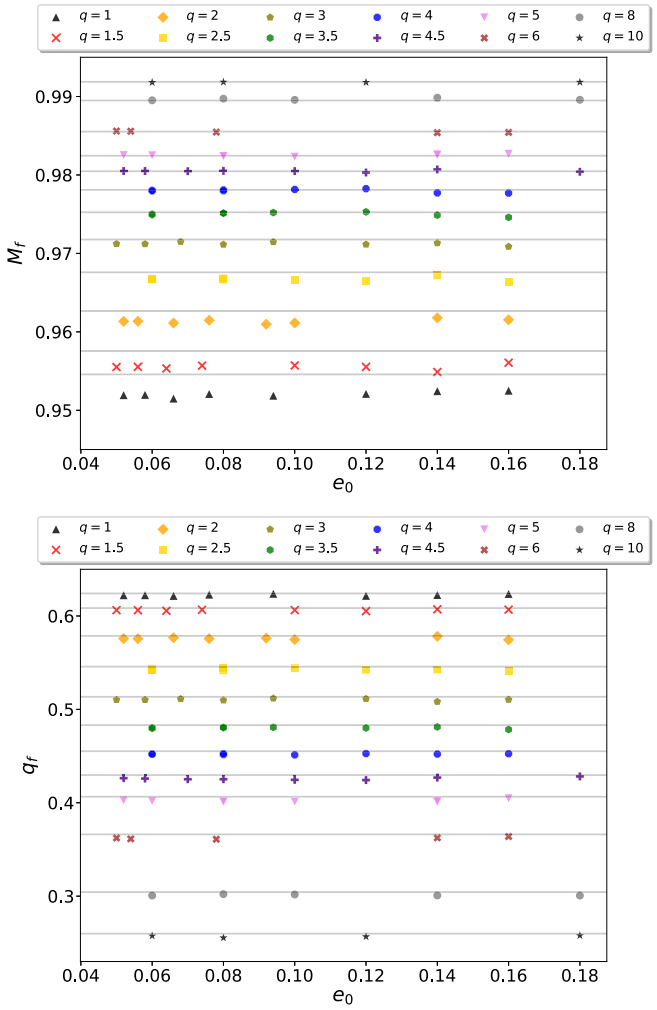

FIG. 3. Final mass, M_f (top panel) and final spin, q_f (bottom panel) of the black hole remnant as a function of the initial eccentricity, e_0, and mass ratio, q, of the binary black hole systems listed in Table II.

the final mass and spin of the BH remnant are nearly independent of eccentricity in the range $e_0 \leq 0.2$. We conclude this since both (M_f, q_f) can be described as constant polynomials in eccentricity within the range we have considered in this study. We can directly compare these results using formulas derived for quasicircular BBH mergers in [113,114]. Notice that we have included horizontal gray lines in both panels that provide the predictions for (M_f, q_f) in the $e_0 \to 0$ limit.

For the M_f results (top panel in Fig. 3) the gray lines present the quasicircular prediction for the final mass of the BH remnant for the mass ratios $q = \{1, 1.5, 2, 2.5, 3, 3.5, 4, 4.5, 5, 6, 8, 10\}$ from bottom to top, respectively. We notice that the equal mass-eccentric BBH population presents the largest deviation from the quasicircular prediction. However, this discrepancy is $\lesssim 1\%$. In the case of the final spin of the BH remnant, the bottom panel of Fig. 3 also presents the quasicircular predictions

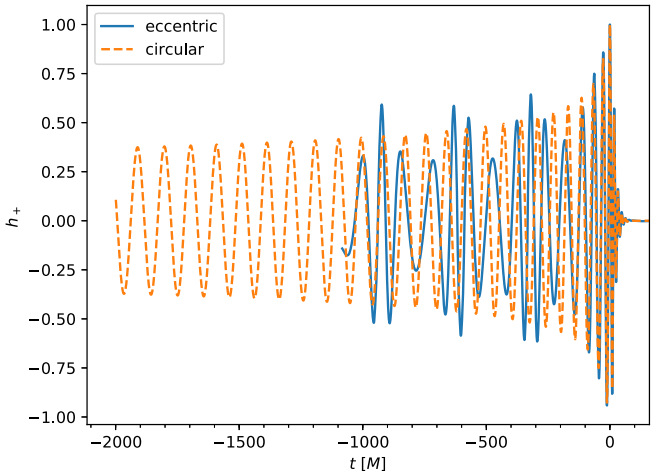

FIG. 4. Waveform signals produced by $q = 10$ BBHs that have the same orbital separation, but different initial eccentricity. We notice that even though the eccentric system has a large initial eccentricity, $e_0 = 0.18$ fifteen cycles before merger, the waveform signal a few cycles before merger is consistent with a quasicircular BBH system.

for this observable. Notice, however, that in this case, the grey lines describe the mass ratios listed above but now from top to bottom. As in the case of M_f, our results for the final spin of moderately eccentric BBH mergers are fairly consistent with results obtained from quasicircular BBH mergers. This can be the case only if the eccentric NR waveforms we have produced in this catalog circularize prior to merger. We have explored this scenario in detail and have found that this is indeed the case. For a sample case, Fig. 4 presents two waveform signals produced by BHs that have the same separation, but different initial eccentricity. The eccentric waveform contains all the telltale signatures of eccentricity, i.e., significant modulations in the amplitude and phase at early times, which correspond to periapse (local maxima) and apoapse (local minima) passages. We also observe that the waveform circularizes very rapidly, from $e_0 = 0.18$ fifteen cycles before merger, turning into a quasicircular waveform signal near the merger event. This is the reason why the results presented in Fig. 3 are consistent with their quasicircular counterparts.

Earlier work on this front includes [115], which presented calculations for the final spin and circularization of equal-mass eccentric BBH mergers, and showed that for BBH mergers with larger initial eccentricities than those considered in this work, the final spin of the BH remnant is greater than its quasicircular counterpart. Additionally, Ref. [31] discussed the circularization of moderately eccentric BBH mergers with $q \leq 3$. In this article, we provide a systematic study of the observables (q_f, M_f) to furnish evidence for the circularization of eccentric BBH mergers with $q \leq 10$ and $e_0 \lesssim 0.18$ fifteen cycles before merger.

TABLE I. From left to right, the mass ratio of binary black hole mergers, q, the recoil velocity of quasicircular binary black hole mergers, $|v|^{e_0\to 0}_{\rm kick}$, and the MINIMUM and MAXIMUM recoil velocities of our numerical relativity catalog for a given mass-ratio population, $[|v|^{\rm min}_{\rm kick}, |v|^{\rm max}_{\rm kick}]$.

q	$\lvert v\rvert^{e_0\to 0}_{\rm kick}$[km/s]	$[\lvert v\rvert^{\rm min}_{\rm kick}, \lvert v\rvert^{\rm max}_{\rm kick}]$[km/s]
1.0	0.0	[0.0, 0.0] [0.0, 0.0]
1.5	107.4	[94.6, 101.8] [104.0, 109.9]
2.0	156.7	[136.9, 149.0] [115.1, 157.5]
2.5	173.5	[152.8, 165.0] [132.9, 180.7]
3.0	174.1	[161.4, 170.9] [151.8, 179.1]
3.5	167.1	[154.4, 173.7] [144.0, 178.8]
4.0	156.9	[143.1, 166.8] [140.0, 173.8]
4.5	145.6	[137.9, 154.6] [133.6, 157.1]
5.0	134.4	[121.0, 137.1] [117.6, 136.8]
6.0	113.9	[99.5, 121.0] [104.5, 121.3]
8.0	82.7	[88.7, 96.5] [70.6, 90.4]
10.0	61.9	[47.0, 78.6] [53.9, 66.4]

We have also computed the recoil velocity of eccentric BBH mergers, $|v|_{\rm kick}$, using the PUNCTURETRACKER thorn in the EINSTEIN TOOLKIT. To do this, we have considered the last 100M of evolution of our NR simulations, and a simple first order finite difference formula for the velocity in terms of the measured locations. In Table I we present the minima and maxima of the recoil velocity, $|v|_{\rm kick}$, for the range of eccentricities we consider for each mass ratio. We have also obtained gauge-invariant perturbations following [116] [see Eqs. (33)–(39) therein]. These gauge-invariant results are presented in the last column of Table I.

Important observations to be drawn from Table I include: (i) the kick velocity of BH remnants produced by quasicircular BH mergers, $|v|^{e_0\to 0}_{\rm kick}$, was obtained using the formulas presented in [117]; (ii) the recoil velocity for all the $q = 1$ eccentric BBH mergers in our catalog is $|v|_{\rm kick} = 0$, which is consistent with results obtained for nonspinning, quasicircular BBH mergers [118]; (iii) the kick velocities for our $1 \leq q \leq 10$ population of eccentric BBH mergers are fairly consistent with the expected values of their quasicircular counterparts, even though the formulas used to estimate $|v|^{e_0\to 0}_{\rm kick}$ was calibrated with quasicircular BBH mergers with mass ratios $q \leq 8$.

These results for $(M_f, q_f, |v|_{\rm kick})$ cover an entirely new region of parameter space in the modeling of eccentric BBH mergers, providing new insights into the physics of these GW sources. We discuss the implications of these findings in the following section.

V. IMPLICATIONS FOR THE MODELING AND DETECTION OF ECCENTRIC MERGERS

To date, there are only a handful of inspiral-merger-ringdown waveform models that describe the GW emission of eccentric BBH mergers [26,29,31,119,120]. These

models assume that moderately eccentric BBHs circularize prior to the merger event. This assumption is sound, in light of the results presented in the previous section, for BBHs with $q \leq 10$ and whose residual eccentricity is as high as $e_0 \leq 0.18$ just fifteen cycles before merger.

Furthermore, we have found that for the most extreme sample of our NR catalog, e.g., P0024, which represents BBHs with $q = 10$ and $e_0 = 0.18$ fifteen cycles before merger, circularization is only attained right before merger, as shown in Fig. 4. In different words, while assuming circularization of moderately eccentric BBH mergers is a reasonable *ansatz*, this also means that the modeling of these GW sources demands the development of an inspiral evolution scheme that provides an accurate description of the dynamical evolution of these objects throughout the inspiral evolution, and which remains accurate one or two cycles before merger. To accomplish this level of accuracy so late in the inspiral evolution, we showed in [26,29] that the inspiral evolution should include, at the very least, higher-order eccentric post-Newtonian corrections for the instantaneous, tails, and tails-of-tails pieces, as well as contributions due to nonlinear memory, and higher-order self-force and BH perturbation theory corrections.

Future source modeling efforts to describe the inspiral evolution of spinning BBHs on eccentric orbits should include new developments from post-Newtonian, self-force, and perturbation theory formalisms [119,121–137]. These schemes may be complemented with stand-alone merger models designed with machine learning, or by directly attaching merger waveforms from NR surrogate waveform families [26,138–143]. The validation of these models with eccentric NR simulations will be essential to assess their accuracy and reliability for the detection and characterization of compact binary populations in dense stellar environments.

This waveform catalog may also be used to assess the sensitivity of burst searches to detect eccentric BBH mergers [80,144–147], and to train neural network models to detect and characterize these GW sources [22,23,27]. These studies will be pursued using this NR waveform catalog.

VI. CONCLUSION

We have studied the physics of eccentric BBH mergers using a NR waveform catalog that describes BBH systems with mass ratios $q \leq 10$ and initial eccentricities $e \leq 0.18$ up to fifteen cycles before merger.

We quantified the importance of including higher-order waveform modes to compute the energy and angular momentum carried away by GWs in eccentric BBH mergers. We have also demonstrated that the properties of BH remnants described by our NR catalog are consistent with their quasicircular counterparts, which provides evidence for the circularization of moderately eccentric BBH mergers. We have also computed recoil velocities of BH remnants produced by eccentric BBH mergers and found that these are fairly similar to those computed in the literature for nonspinning, quasicircular BBH mergers.

Based on these analyses, we have provided evidence that existing source modeling efforts that assume the circularization of moderately eccentric BBH mergers is sound. We have also shown that since circularization takes place close to the merger event, any semianalytical model that is used to describe these GW sources should include higher-order corrections to both the conservative and the radiative pieces of the source's dynamics, and to the waveform strain.

Recent studies in the literature have identified parameter space degeneracies between orbital eccentricity and spin corrections [29]. In order to get better insights into this finding, it is essential to understand the dynamics of spinning BHs on eccentric orbits, and then use the NR waveform catalog we have introduced in this study to carefully assess in which regions of parameter space such a degeneracy may be broken to distinguish these two compact binary populations.

The construction of a NR waveform catalog for spinning BHs on eccentric orbits is already underway to shed light on this timely and astrophysically motivated study. Specific aspects to address in such a study will encompass: (i) orbital configurations that significantly shorten the length of waveform signals, i.e., eccentricity and spin antialigned configurations; (ii) competing effects to determine the length of waveform signals, i.e., rapidly spinning BHs on spin-aligned configurations (which increase the length of waveforms as compared to nonspinning BBHs) vs moderate values of initial eccentricity (which decrease the length of waveforms as compared to quasicircular BBHs); and (iii) identify telltale signatures of GW sources that can be used to infer the existence of eccentric compact binary populations through GW observations, e.g., astrophysical properties of the BH remnant, and the coupling of eccentricity and spin-spin and spin-orbit effects at periapse passages during the inspiral evolution of these systems.

The modes we have extracted in this study with the open source POWER [103] package do not include $m = 0$ memory modes. Their extraction requires the use of the Cauchy characteristic extraction method [148]. Given the importance of these modes for the characterization of eccentric BBH mergers, we will present these modes in a forthcoming study, accompanied by a systematic analysis on the observability of these modes with second and third generation GW detectors.

ACKNOWLEDGMENTS

This research is part of the Blue Waters sustained petascale computing project, which is supported by the National Science Foundation (NSF), Awards No. OCI-0725070 and No. ACI-1238993, and the State of Illinois. Blue Waters is a joint effort of the University of Illinois at Urbana-Champaign and its National Center for

Supercomputing Applications (NCSA). We acknowledge support from the NCSA and the SPIN Program at NCSA. We thank the `NCSA Gravity Group` [149] for useful feedback. NSF-1550514, NSF-1659702, NSF-OAC1659702, and TG-PHY160053 grants are gratefully acknowledged. This research used resources of the Argonne Leadership Computing Facility, which is a DOE Office of Science User Facility supported under Contract No. DE-AC02-06CH11357.

APPENDIX A: PROPERTIES OF NUMERICAL RELATIVITY CATALOG

Table II lists the properties of our numerical relativity catalog.

TABLE II. (e_0, ℓ_0, x_0) represent the measured values of eccentricity, mean anomaly, and dimensionless orbital frequency parameters. These quantities are computed upon removing the first $60M$ of evolution of the numerical relativity waveforms, as described in [105].

Simulation	q	e_0	ℓ_0	x_0
E0001	1	0.052	3.0	0.0770
E0009	2	0.052	3.0	0.0794
E0013	2.5	0.050	3.0	0.0813
E0017	3	0.050	3.0	0.0831
F0002	1	0.066	3.0	0.0780
F0010	2	0.066	3.0	0.0803
F0014	2.5	0.068	3.0	0.0822
F0018	3	0.068	3.0	0.0842
G0003	1	0.094	3.0	0.0788
H0004	1	0.140	3.0	0.0826
H0011	2	0.092	3.0	0.0795
H0015	2.5	0.094	3.0	0.0812
H0019	3	0.094	3.0	0.0832
I0004	1	0.140	3.0	0.0765
I0012	2	0.140	3.0	0.0791
I0016	2.5	0.140	3.0	0.0811
I0020	3	0.140	3.0	0.0824
I0028	4	0.140	2.9	0.0865
J0005	1.5	0.050	3.0	0.0779
J0006	1.5	0.064	3.0	0.0782
J0007	1.5	0.100	3.1	0.0762
J0008	1.5	0.140	3.0	0.0768
J0037	1	0.058	3.0	0.0768
J0038	1	0.076	3.0	0.0762
J0039	1	0.120	3.1	0.0749
J0040	1	0.160	3.0	0.0761
J0041	1.5	0.056	3.0	0.0777
J0042	1.5	0.074	3.0	0.0771
J0043	1.5	0.120	3.1	0.0756
J0044	1.5	0.160	2.9	0.0778
J0045	2	0.056	3.0	0.0793
J0046	2	0.076	3.0	0.0787
J0047	2	0.100	3.0	0.0778
J0048	2	0.160	2.9	0.0794
J0049	2.5	0.058	3.0	0.0811
J0050	2.5	0.078	3.0	0.0806
J0051	2.5	0.120	3.0	0.0795
J0052	2.5	0.160	2.9	0.0817
J0053	3	0.058	3.0	0.0829
J0054	3	0.080	3.0	0.0823
J0055	3	0.120	3.0	0.0816
J0056	3	0.160	2.9	0.0829
J0061	4	0.060	3.0	0.0855
J0062	4	0.080	3.1	0.0847
J0063	4	0.120	3.0	0.0841
J0064	4	0.160	2.9	0.0863
J0065	4.5	0.058	3.0	0.0878
J0066	4.5	0.080	3.0	0.0870
J0067	4.5	0.120	3.0	0.0858
J0068	4.5	0.180	2.9	0.0874
K0001	3.5	0.060	3.0	0.0802
K0002	3.5	0.080	3.0	0.0808
K0003	3.5	0.094	3.1	0.0800
K0004	3.5	0.140	3.0	0.0810
K0005	4.0	0.054	3.0	0.0817
K0006	4.0	0.068	3.0	0.0826
K0007	4.0	0.094	3.0	0.0823
K0008	4.0	0.140	2.9	0.0833
K0016	5.0	0.140	2.9	0.0868
K0017	3.5	0.060	3.0	0.0801
K0018	3.5	0.080	3.1	0.0801
K0019	3.5	0.120	3.1	0.0789
K0020	3.5	0.160	2.9	0.0829
K0021	4.0	0.060	3.0	0.0821
K0022	4.0	0.080	3.0	0.0823
K0023	4.0	0.120	3.0	0.0817
K0024	4.0	0.160	2.9	0.0856
K0032	5.0	0.160	2.8	0.0888
L0009	4.5	0.052	3.0	0.0839
L0010	4.5	0.070	3.0	0.0841
L0011	4.5	0.100	3.0	0.0837
L0012	4.5	0.140	2.9	0.0849
L0013	5.0	0.052	3.0	0.0854
L0014	5.0	0.080	3.0	0.0856
L0015	5.0	0.100	3.0	0.0853
L0016	5.0	0.140	2.9	0.0862
L0017	5.5	0.060	3.0	0.0869
L0018	5.5	0.068	3.0	0.0878
L0019	5.5	0.100	3.0	0.0869
L0020	5.5	0.140	2.9	0.0882
L0029	4.5	0.058	3.0	0.0844
L0030	4.5	0.080	3.1	0.0835
L0031	4.5	0.120	3.1	0.0827
L0032	4.5	0.180	3.0	0.0849
L0033	5.0	0.060	3.0	0.0852
L0034	5.0	0.080	3.0	0.0852
L0037	5.5	0.060	3.0	0.0870
L0038	5.5	0.080	3.0	0.0870

TABLE II. *(Continued)*

Simulation	q	e_0	ℓ_0	x_0
L0039	5.5	0.120	2.9	0.0867
L0040	5.5	0.180	2.9	0.0894
P0001	6	0.050	3.0	0.0867
P0004	6	0.140	2.9	0.0867
P0006	8	0.080	2.9	0.0931
P0007	8	0.100	2.9	0.0926
P0008	8	0.140	2.9	0.0910
P0009	10	0.060	2.9	0.0971
P0013	6	0.054	3.0	0.0871
P0014	6	0.078	2.9	0.0885
P0016	6	0.160	2.8	0.0900
P0017	8	0.060	3.0	0.0927
P0020	8	0.180	2.9	0.0936
P0022	10	0.080	2.9	0.0979
P0023	10	0.120	2.9	0.0968
P0024	10	0.180	3.0	0.0957

APPENDIX B: CONVERGENCE OF THE NUMERICAL WAVEFORMS

We use a grid setup based on the setup used in [89]. There is a central, mesh refined cubical region of the grid in which Cartesian coordinates are used, surrounded by six regions that make up a cubed sphere grid with constant angular resolution.

We use eighth order finite differencing operators to compute spatial derivatives of the spacetime quantities in the Einstein field equations. This requires the use of five ghost zones, and together with using a classical fourth order Runge-Kutta time stepper implies that each refined region is surrounded by 20 points that are filled in via prolongation from the next coarser region. We use vertex centered fifth order prolongation operators rather than full eighth order prolongation operators.

The cubical region employs mesh refinement with the resolution on the coarsest grid being $h_{\rm coarse} = 1.92M$. Each of the black holes is surrounded by a set of nested moving boxes such that the resolution in the finest box containing the black hole i is $1.2M_i/(N_l - 1)$ where M_i is the initial mass parameter of black hole i and N_l is the number of points used for the resolution level l simulation. In our simulations we used $N_l = 32$, 36, 40, 44, where $N_l = 44$ was only used for simulations with a mass ratio $q > 5$. The finest box surrounding each black hole has a radius of $1.2M_i$ and each coarser box has twice the radius of the next finer one. During the simulation we track the location of each black hole and keep the set of nested refined boxes approximately centered on the black hole. Finally the outer edge of the cubical region is chosen large enough to contain all refined regions including their prolongation regions.

In the spherical region we choose an angular resolution of $h_{\rm angular} = \pi/(4N_l)$ and a radial resolution of $1.92M$ which matches the coarsest resolution in the Cartesian grid. The outer boundary is chosen such that it is causally disconnected from the outermost detector at which we extract gravitational waves from.

We use a time step $\Delta t = 0.864M$ on the coarsest level, corresponding to a Courant-Friedrichs-Lewy condition of $\Delta t/h_{\rm coarse} = 0.45$ which is held constant on the finer levels by decreasing their time step size.

We extract gravitational waves using modes of the Weyl scalar ψ_4 extracted on coordinate spheres of radius $r_{{\rm det},i} = 100M, 115M, 136M, 167M, 214M, 300M, 500M$.

Using eighth order finite differencing operators our simulations would, under ideal circumstances, converge toward the correct solution with an error term which scales like h^8, where h is the spatial resolution of the simulation. However, due to lower order schemes present in the simulation, for example the interpolation at mesh refinement boundaries which is only fifth order accurate, as well as artifacts caused by the adaptive mesh refinement logic making independent decisions where to refine for each simulation, the observed convergence order typically differs from eight.

To estimate the convergence of each waveform we simulated each set of physical parameters using at least three (four) simulations using increasing resolution for waveforms of mass ratio $q \leq 5$ ($q > 5$). We then compute the gravitational wave phase $\phi^{(2,2)}$ from the complex $\ell = m = 2$ mode of the spherical harmonic decomposition of the outgoing component of the Weyl scalar ψ_4 and studied its convergence properties.

Figure 5 shows the rescaled phase differences $\phi^{(2,2)}(h_n) - \phi^{(2,2)}(h_{\rm high})$ between the gravitational wave phase obtained from the simulation with resolution h_n and the highest resolved simulation. Phase differences have been rescaled

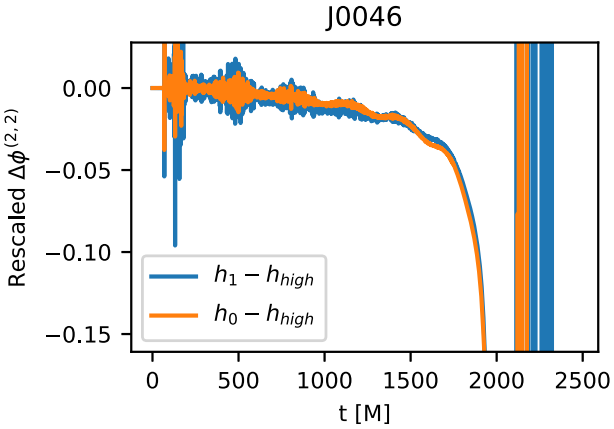

FIG. 5. Convergence of the phase difference in the gravitational wave phase for case J0046, rescaled to demonstrate convergence at order $N \approx 4.5$. We compute convergence in the time interval $500M \leq t \leq t_{\rm max} - 200M$, where $t_{\rm max}$ is the point of maximum amplitude, approximately corresponding to the time of merger. Note that this plot includes the pulse of junk radiation due to our initial data not containing any waves as well as the ringdown and merger signal, both of which are not convergent and thus lead to very large phase differences which are clipped in the plot.

such that for a convergent simulation the plotted curves overlap. For case `J0046` we observe an approximate convergence order of $N \approx 4.5$ which is within the range of expected values.

Not all simulated cases show clean convergence behavior, with the convergence order for some of them being larger than eight, which may indicate that our lowest resolution simulation does not adequately resolve the features present in the simulation domain, and others swapping the ordering of phases between the low, medium, and high resolution simulations, making an estimate of the convergence order impossible.

Given that large number of simulations, this is to be expected and does not necessarily indicate that the obtained results are incorrect but instead demonstrates the difficulty in controlling the various effects that influence the numerically obtained waveform. Since there are multiple sources of numerical error, and we have chosen parameters such that none is dominant so as to make best use of available computing resources without overresolving a particular feature, different sources of numerical error potentially cancel each other out, giving rise to unrealistically large (or small) convergence orders.

[1] B. P. Abbott, R. Abbott, T. D. Abbott, M. R. Abernathy, F. Acernese, K. Ackley, C. Adams, T. Adams, P. Addesso, R. X. Adhikari *et al.*, Phys. Rev. Lett. **116**, 061102 (2016).

[2] B. P. Abbott, R. Abbott, T. D. Abbott, M. R. Abernathy, F. Acernese, K. Ackley, C. Adams, T. Adams, P. Addesso, R. X. Adhikari *et al.*, Phys. Rev. Lett. **116**, 241103 (2016).

[3] B. P. Abbott, R. Abbott, T. D. Abbott, M. R. Abernathy, F. Acernese, K. Ackley, C. Adams, T. Adams, P. Addesso, R. X. Adhikari *et al.*, Phys. Rev. Lett. **118**, 221101 (2017).

[4] B. P. Abbott, R. Abbott, T. D. Abbott, F. Acernese, K. Ackley, C. Adams, T. Adams, P. Addesso, R. X. Adhikari, V. B. Adya *et al.*, Phys. Rev. Lett. **119**, 141101 (2017).

[5] B. P. Abbott, R. Abbott, T. D. Abbott, F. Acernese, K. Ackley, C. Adams, T. Adams, P. Addesso, R. X. Adhikari, V. B. Adya *et al.*, Astrophys. J. Lett. **851**, L35 (2017).

[6] LIGO Scientific and Virgo Collaborations, arXiv: 1811.12907.

[7] B. P. Abbott, R. Abbott, T. D. Abbott, F. Acernese, K. Ackley, C. Adams, T. Adams, P. Addesso, R. X. Adhikari, V. B. Adya *et al.*, Phys. Rev. Lett. **119**, 161101 (2017).

[8] B. P. Abbott, R. Abbott, T. D. Abbott, F. Acernese, K. Ackley, C. Adams, T. Adams, P. Addesso, R. X. Adhikari, V. B. Adya *et al.*, Astrophys. J. Lett. **848**, L12 (2017).

[9] D. A. Coulter, R. J. Foley, C. D. Kilpatrick, M. R. Drout, A. L. Piro, B. J. Shappee, M. R. Siebert, J. D. Simon, N. Ulloa, D. Kasen, B. F. Madore, A. Murguia-Berthier, Y.-C. Pan, J. X. Prochaska, E. Ramirez-Ruiz, A. Rest, and C. Rojas-Bravo, Science **358**, 1556 (2017).

[10] LIGO Scientific and Virgo Collaborations, Astrophys. J. **850**, L39 (2017).

[11] B. P. Abbott, R. Abbott, T. D. Abbott, F. Acernese, K. Ackley, C. Adams, T. Adams, P. Addesso, R. X. Adhikari, V. B. Adya *et al.*, Astrophys. J. Lett. **848**, L13 (2017).

[12] B. P. Abbott *et al.*, Nature (London) **551**, 85 (2017).

[13] M. Fishbach, R. Gray, I. Magaña Hernandez, H. Qi, and A. Sur (LIGO Scientific and Virgo Collaboration), Astrophys. J. **871**, L13 (2019).

[14] B. F. Schutz, Nature (London) **323**, 310 (1986).

[15] D. E. Holz and S. A. Hughes, Astrophys. J. **629**, 15 (2005).

[16] T. Chu, H. Fong, P. Kumar, H. P. Pfeiffer, M. Boyle, D. A. Hemberger, L. E. Kidder, M. A. Scheel, and B. Szilagyi, Classical Quantum Gravity **33**, 165001 (2016).

[17] A. H. Mroué, M. A. Scheel, B. Szilágyi, H. P. Pfeiffer, M. Boyle, D. A. Hemberger, L. E. Kidder, G. Lovelace, S. Ossokine, N. W. Taylor, A. Zenginoğlu, L. T. Buchman, T. Chu, E. Foley, M. Giesler, R. Owen, and S. A. Teukolsky, Phys. Rev. Lett. **111**, 241104 (2013).

[18] P. Kumar, T. Chu, H. Fong, H. P. Pfeiffer, M. Boyle, D. A. Hemberger, L. E. Kidder, M. A. Scheel, and B. Szilagyi, Phys. Rev. D **93**, 104050 (2016).

[19] B. P. Abbott, R. Abbott, T. D. Abbott, M. R. Abernathy, F. Acernese, K. Ackley, C. Adams, T. Adams, P. Addesso, R. X. Adhikari *et al.*, Phys. Rev. D **94**, 064035 (2016).

[20] LIGO Scientific and Virgo Collaborations, Classical Quantum Gravity **34**, 104002 (2017).

[21] J. Lange *et al.*, Phys. Rev. D **96**, 104041 (2017).

[22] D. George and E. A. Huerta, Phys. Rev. D **97**, 044039 (2018).

[23] D. George and E. A. Huerta, Phys. Lett. B **778**, 64 (2018).

[24] H. Shen, D. George, E. A. Huerta, and Z. Zhao, arXiv:1711.09919.

[25] D. George, H. Shen, and E. A. Huerta, Phys. Rev. D **97**, 101501 (2018).

[26] E. A. Huerta, C. J. Moore, P. Kumar, D. George, A. J. K. Chua, R. Haas, E. Wessel, D. Johnson, D. Glennon, A. Rebei, A. M. Holgado, J. R. Gair, and H. P. Pfeiffer, Phys. Rev. D **97**, 024031 (2018).

[27] A. Rebei, E. A. Huerta, S. Wang, S. Habib, R. Haas, D. Johnson, and D. George, Phys. Rev. D **100**, 044025 (2019).

[28] I. Hinder, F. Herrmann, P. Laguna, and D. Shoemaker, Phys. Rev. D **82**, 024033 (2010).

[29] E. A. Huerta, P. Kumar, B. Agarwal, D. George, H.-Y. Schive, H. P. Pfeiffer, R. Haas, W. Ren, T. Chu, M. Boyle, D. A. Hemberger, L. E. Kidder, M. A. Scheel, and B. Szilagyi, Phys. Rev. D **95**, 024038 (2017).

[30] U. Sperhake, E. Berti, V. Cardoso, J. A. González, B. Brügmann, and M. Ansorg, Phys. Rev. D **78**, 064069 (2008).
[31] I. Hinder, L. E. Kidder, and H. P. Pfeiffer, Phys. Rev. D **98**, 044015 (2018).
[32] C. D. Ott, Classical Quantum Gravity **26**, 063001 (2009).
[33] K. Kotake, C. R. Phys. **14**, 318 (2013).
[34] T. Hinderer, S. Nissanke, F. Foucart, K. Hotokezaka, T. Vincent, M. Kasliwal, P. Schmidt, A. R. Williamson, D. Nichols, M. Duez, L. E. Kidder, H. P. Pfeiffer, and M. A. Scheel, arXiv:1808.03836.
[35] F. Foucart, M. D. Duez, T. Hinderer, J. Caro, A. R. Williamson, M. Boyle, A. Buonanno, R. Haas, D. A. Hemberger, L. E. Kidder, H. P. Pfeiffer, and M. A. Scheel, Phys. Rev. D **99**, 044008 (2019).
[36] D. Radice, V. Morozova, A. Burrows, D. Vartanyan, and H. Nagakura, Astrophys. J. **876**, L9 (2019).
[37] J. Healy, C. O. Lousto, Y. Zlochower, and M. Campanelli, Classical Quantum Gravity **34**, 224001 (2017).
[38] K. Jani, J. Healy, J. A. Clark, L. London, P. Laguna, and D. Shoemaker, Classical Quantum Gravity **33**, 204001 (2016).
[39] C. J. Hailey, K. Mori, F. E. Bauer, M. E. Berkowitz, J. Hong, and B. J. Hord, Nature (London) **556**, 70 (2018).
[40] A. C. Sippel and J. R. Hurley, Mon. Not. R. Astron. Soc. **430**, L30 (2013).
[41] J. Strader, L. Chomiuk, T. J. Maccarone, J. C. A. Miller-Jones, and A. C. Seth, Nature (London) **490**, 71 (2012).
[42] J. Samsing, D. J. D'Orazio, A. Askar, and M. Giersz, arXiv:1802.08654.
[43] L. Blanchet, Living Rev. Relativity **17**, 2 (2014).
[44] J. Samsing and E. Ramirez-Ruiz, Astrophys. J. Lett. **840**, L14 (2017).
[45] J. Samsing, M. MacLeod, and E. Ramirez-Ruiz, Astrophys. J. **784**, 71 (2014).
[46] J. Samsing, Phys. Rev. D **97**, 103014 (2018).
[47] N. W. C. Leigh, A. M. Geller, B. McKernan, K. E. S. Ford, M. M. Mac Low, J. Bellovary, Z. Haiman, W. Lyra, J. Samsing, M. O'Dowd, B. Kocsis, and S. Endlich, Mon. Not. R. Astron. Soc. **474**, 5672 (2018).
[48] J. Samsing, A. Askar, and M. Giersz, Astrophys. J. **855**, 124 (2018).
[49] J. Samsing, M. MacLeod, and E. Ramirez-Ruiz, Astrophys. J. **853**, 140 (2018).
[50] L. Randall and Z.-Z. Xianyu, Astrophys. J. **853**, 93 (2018).
[51] E. A. Huerta and J. R. Gair, Phys. Rev. D **79**, 084021 (2009).
[52] J. Samsing, M. MacLeod, and E. Ramirez-Ruiz, Astrophys. J. **846**, 36 (2017).
[53] J. Samsing and T. Ilan, Mon. Not. R. Astron. Soc. **476**, 1548 (2018).
[54] E. A. Huerta, S. T. McWilliams, J. R. Gair, and S. R. Taylor, Phys. Rev. D **92**, 063010 (2015).
[55] J. Samsing and T. Ilan, Mon. Not. R. Astron. Soc. **482**, 30 (2019).
[56] J. Samsing, N. W. C. Leigh, and A. A. Trani, Mon. Not. R. Astron. Soc. **481**, 5436 (2018).
[57] E. A. Huerta, P. Kumar, S. T. McWilliams, R. O'Shaughnessy, and N. Yunes, Phys. Rev. D **90**, 084016 (2014).
[58] F. Antonini, N. Murray, and S. Mikkola, Astrophys. J. **781**, 45 (2014).
[59] J. Samsing and D. J. D'Orazio, Mon. Not. R. Astron. Soc. **481**, 5445 (2018).
[60] D. J. D'Orazio and J. Samsing, Mon. Not. R. Astron. Soc. **481**, 4775 (2018).
[61] J. Samsing and D. J. D'Orazio, Phys. Rev. D **99**, 063006 (2019).
[62] M. Zevin, J. Samsing, C. Rodriguez, C.-J. Haster, and E. Ramirez-Ruiz, Astrophys. J. **871**, 91 (2019).
[63] C. L. Rodriguez, P. Amaro-Seoane, S. Chatterjee, K. Kremer, F. A. Rasio, J. Samsing, C. S. Ye, and M. Zevin, Phys. Rev. D **98**, 123005 (2018).
[64] K. Kremer, C. L. Rodriguez, P. Amaro-Seoane, K. Breivik, S. Chatterjee, M. L. Katz, S. L. Larson, F. A. Rasio, J. Samsing, C. S. Ye, and M. Zevin, Phys. Rev. D **99**, 063003 (2019).
[65] J. Lopez, Martin, A. Batta, E. Ramirez-Ruiz, I. Martinez, and J. Samsing, Astrophys. J. **877**, 56 (2019).
[66] B.-M. Hoang, S. Naoz, B. Kocsis, F. A. Rasio, and F. Dosopoulou, Astrophys. J. **856**, 140 (2018).
[67] L. Gondán, B. Kocsis, P. Raffai, and Z. Frei, Astrophys. J. **855**, 34 (2018).
[68] B.-M. Hoang, S. Naoz, B. Kocsis, F. A. Rasio, and F. Dosopoulou, Astrophys. J. **856**, 140 (2018).
[69] L. Randall and Z.-Z. Xianyu, Astrophys. J. **864**, 134 (2018).
[70] B. Mikóczi, B. Kocsis, P. Forgács, and M. Vasúth, Phys. Rev. D **86**, 104027 (2012).
[71] S. Naoz, B. Kocsis, A. Loeb, and N. Yunes, Astrophys. J. **773**, 187 (2013).
[72] L. Gondán and B. Kocsis, Astrophys. J. **871**, 178 (2019).
[73] F. Antonini and F. A. Rasio, Astrophys. J. **831**, 187 (2016).
[74] E. A. Huerta and D. A. Brown, Phys. Rev. D **87**, 127501 (2013).
[75] M. Arca-Sedda, G. Li, and B. Kocsis, arXiv:1805.06458.
[76] Á. Takács and B. Kocsis, Astrophys. J. **856**, 113 (2018).
[77] L. Gondán, B. Kocsis, P. Raffai, and Z. Frei, Astrophys. J. **860**, 5 (2018).
[78] F. Antonini, M. Gieles, and A. Gualandris, Mon. Not. R. Astron. Soc. **486**, 5008 (2019).
[79] F. Antonini, S. Chatterjee, C. L. Rodriguez, M. Morscher, B. Pattabiraman, V. Kalogera, and F. A. Rasio, Astrophys. J. **816**, 65 (2016).
[80] S. Klimenko, G. Vedovato, M. Drago, F. Salemi, V. Tiwari, G. A. Prodi, C. Lazzaro, K. Ackley, S. Tiwari, C. F. Da Silva, and G. Mitselmakher, Phys. Rev. D **93**, 042004 (2016).
[81] http://einsteintoolkit.org.
[82] F. Loffler *et al.*, Classical Quantum Gravity **29**, 115001 (2012).
[83] T. Nakamura, K. Oohara, and Y. Kojima, Prog. Theor. Phys. Suppl. **90**, 1 (1987).
[84] M. Shibata and T. Nakamura, Phys. Rev. D **52**, 5428 (1995).
[85] T. W. Baumgarte and S. L. Shapiro, Phys. Rev. D **59**, 024007 (1998).
[86] J. G. Baker, J. Centrella, D.-I. Choi, M. Koppitz, and J. van Meter, Phys. Rev. Lett. **96**, 111102 (2006).

[87] M. Campanelli, C. O. Lousto, P. Marronetti, and Y. Zlochower, Phys. Rev. Lett. **96**, 111101 (2006).
[88] D. Pollney, C. Reisswig, E. Schnetter, N. Dorband, and P. Diener, Phys. Rev. D **83**, 044045 (2011).
[89] B. Wardell, I. Hinder, and E. Bentivegna, Simulation of GW150914 binary black hole merger using the Einstein Toolkit, https://doi.org/10.5281/zenodo.155394 (2016).
[90] D. Pollney, C. Reisswig, E. Schnetter, N. Dorband, and P. Diener, Phys. Rev. D **83**, 044045 (2011).
[91] M. Thomas and E. Schnetter, in *2010 11th IEEE/ACM International Conference on Grid Computing* (IEEE, New York, 2010), pp. 369–378, https://ieeexplore.ieee.org/document/5698010.
[92] F. Löffler, J. Faber, E. Bentivegna, T. Bode, P. Diener, R. Haas, I. Hinder, B. C. Mundim, C. D. Ott, E. Schnetter, G. Allen, M. Campanelli, and P. Laguna, Classical Quantum Gravity **29**, 115001 (2012).
[93] M. Ansorg, B. Brügmann, and W. Tichy, Phys. Rev. D **70**, 064011 (2004).
[94] P. Diener, E. N. Dorband, E. Schnetter, and M. Tiglio, J. Sci. Comput. **32**, 109 (2007).
[95] O. Dreyer, B. Krishnan, D. Shoemaker, and E. Schnetter, Phys. Rev. D **67**, 024018 (2003).
[96] E. Schnetter, S. H. Hawley, and I. Hawke, Classical Quantum Gravity **21**, 1465 (2004).
[97] J. Thornburg, Classical Quantum Gravity **21**, 743 (2004).
[98] J. D. Brown, P. Diener, O. Sarbach, E. Schnetter, and M. Tiglio, Phys. Rev. D **79**, 044023 (2009).
[99] S. Husa, I. Hinder, and C. Lechner, Comput. Phys. Commun. **174**, 983 (2006).
[100] Kranc, Kranc: Kranc assembles numerical code, http://kranccode.org/.
[101] NCSA Gravity Group, 2019, https://youtu.be/4U5L8EAj2EU.
[102] NCSA Gravity Group, 2019, https://gravity.ncsa.illinois.edu/products/outreach/.
[103] D. Johnson, E. A. Huerta, and R. Haas, Classical Quantum Gravity **35**, 027002 (2018).
[104] J. Healy, C. O. Lousto, H. Nakano, and Y. Zlochower, Classical Quantum Gravity **34**, 145011 (2017).
[105] S. Habib and E. A. Huerta, Phys. Rev. D **100**, 044016 (2019).
[106] A. Bohé, L. Shao, A. Taracchini, A. Buonanno, S. Babak, I. W. Harry, I. Hinder, S. Ossokine, M. Pürrer, V. Raymond, T. Chu, H. Fong, P. Kumar, H. P. Pfeiffer, M. Boyle, D. A. Hemberger, L. E. Kidder, G. Lovelace, M. A. Scheel, and B. Szilágyi, Phys. Rev. D **95**, 044028 (2017).
[107] L. Barsotti, S. Gras, M. Evans, and P. Fritschel, Advanced LIGO anticipated sensitivity curves, 2018, https://dcc.ligo.org/LIGO-T1800044/public.
[108] T. Damour, A. Nagar, D. Pollney, and C. Reisswig, Phys. Rev. Lett. **108**, 131101 (2012).
[109] C. W. Misner, K. S. Thorne, and J. A. Wheeler, *Gravitation* (W.H. Freeman and Co., San Francisco, 1973).
[110] R. M. Wald, *General Relativity* (University of Chicago Press, Chicago, 1984), p. 504.
[111] E. Poisson, *A Relativist's Toolkit: The Mathematics of Black-Hole Mechanics* (Cambridge University Press, Cambridge, England, 2009).
[112] J. L. Jaramillo and E. Gourgoulhon, Fundam. Theor. Phys. **162**, 87 (2011).
[113] J. G. Baker, W. D. Boggs, J. Centrella, B. J. Kelly, S. T. McWilliams, and J. R. van Meter, Phys. Rev. D **78**, 044046 (2008).
[114] F. Hofmann, E. Barausse, and L. Rezzolla, Astrophys. J. **825**, L19 (2016).
[115] I. Hinder, B. Vaishnav, F. Herrmann, D. M. Shoemaker, and P. Laguna, Phys. Rev. D **77**, 081502 (2008).
[116] D. Pollney *et al.*, Phys. Rev. D **76**, 124002 (2007).
[117] C. O. Lousto and Y. Zlochower, Phys. Rev. D **87**, 084027 (2013).
[118] M. Koppitz, D. Pollney, C. Reisswig, L. Rezzolla, J. Thornburg, P. Diener, and E. Schnetter, Phys. Rev. Lett. **99**, 041102 (2007).
[119] T. Hinderer and S. Babak, Phys. Rev. D **96**, 104048 (2017).
[120] Z. Cao and W.-B. Han, Phys. Rev. D **96**, 044028 (2017).
[121] D. Bini, T. Damour, and A. Geralico, Phys. Rev. D **93**, 104017 (2016).
[122] D. Bini, T. Damour, and A. Geralico, Phys. Rev. D **93**, 064023 (2016).
[123] D. Bini and A. Geralico, Phys. Rev. D **98**, 064026 (2018).
[124] D. Bini, T. Damour, and A. Geralico, Phys. Rev. D **97**, 104046 (2018).
[125] C. Kavanagh, D. Bini, T. Damour, S. Hopper, A. C. Ottewill, and B. Wardell, Phys. Rev. D **96**, 064012 (2017).
[126] D. Bini, T. Damour, and A. Geralico, Phys. Rev. D **93**, 124058 (2016).
[127] S. Akcay and M. van de Meent, Phys. Rev. D **93**, 064063 (2016).
[128] S. Akcay, D. Dempsey, and S. R. Dolan, Classical Quantum Gravity **34**, 084001 (2017).
[129] R. Fujita, S. Isoyama, A. Le Tiec, H. Nakano, N. Sago, and T. Tanaka, Classical Quantum Gravity **34**, 134001 (2017).
[130] A. Le Tiec, Phys. Rev. D **92**, 084021 (2015).
[131] T. Osburn, E. Forseth, C. R. Evans, and S. Hopper, Phys. Rev. D **90**, 104031 (2014).
[132] N. Warburton, T. Osburn, and C. R. Evans, Phys. Rev. D **96**, 084057 (2017).
[133] M. van de Meent, Phys. Rev. D **94**, 044034 (2016).
[134] M. van de Meent, Phys. Rev. Lett. **118**, 011101 (2017).
[135] M. van de Meent, Phys. Rev. D **97**, 104033 (2018).
[136] M. van de Meent and N. Warburton, Classical Quantum Gravity **35**, 144003 (2018).
[137] B. Ireland, O. Birnholtz, H. Nakano, E. West, and M. Campanelli, Phys. Rev. D **100**, 024015 (2019).
[138] J. Blackman, S. E. Field, C. R. Galley, B. Szilágyi, M. A. Scheel, M. Tiglio, and D. A. Hemberger, Phys. Rev. Lett. **115**, 121102 (2015).
[139] V. Varma, S. Field, M. A. Scheel, J. Blackman, L. E. Kidder, and H. P. Pfeiffer, Phys. Rev. D **99**, 064045 (2019).
[140] Z. Doctor, B. Farr, D. E. Holz, and M. Pürrer, Phys. Rev. D **96**, 123011 (2017).
[141] C. J. Moore, A. J. K. Chua, C. P. L. Berry, and J. R. Gair, R. Soc. Open Sci. **3**, 160125 (2016).
[142] C. J. Moore, C. P. L. Berry, A. J. K. Chua, and J. R. Gair, Phys. Rev. D **93**, 064001 (2016).

[143] V. Varma, S. E. Field, M. A. Scheel, J. Blackman, D. Gerosa, L. C. Stein, L. E. Kidder, and H. P. Pfeiffer, arXiv:1905.09300.
[144] S. Klimenko, I. Yakushin, M. Rakhmanov, and G. Mitselmakher, Classical Quantum Gravity **21**, S1685 (2004).
[145] S. Klimenko and G. Mitselmakher, Classical Quantum Gravity **21**, S1819 (2004).
[146] S. Klimenko, I. Yakushin, A. Mercer, and G. Mitselmakher, Classical Quantum Gravity **25**, 114029 (2008).
[147] V. Tiwari, S. Klimenko, N. Christensen, E. A. Huerta, S. R. P. Mohapatra, A. Gopakumar, M. Haney, P. Ajith, S. T. McWilliams, G. Vedovato, M. Drago, F. Salemi, G. A. Prodi, C. Lazzaro, S. Tiwari, G. Mitselmakher, and F. Da Silva, Phys. Rev. D **93**, 043007 (2016).
[148] C. Reisswig, N. T. Bishop, D. Pollney, and B. Szilagyi, Classical Quantum Gravity **27**, 075014 (2010).
[149] http://gravity.ncsa.illinois.edu.